CHAPTER 5

PHOTOACOUSTIC TECHNIQUE FOR THERMAL CONDUCTIVITY AND THERMAL INTERFACE MEASUREMENTS

Xinwei Wang,[1] Baratunde A. Cola,[2,3] Thomas L. Bougher,[2] Stephen L. Hodson,[4] Timothy S. Fisher,[4] & Xianfan Xu[4,]*

[1] Department of Mechanical Engineering, Iowa State University, Ames, IA, USA

[2] Department of Mechanical Engineering, Georgia Institute of Technology, Atlanta, GA, USA

[3] School of Materials Science and Engineering, Georgia Institute of Technology, Atlanta, GA, USA

[4] School of Mechanical Engineering and Birck Nanotechnology Center, Purdue University, West Lafayette, IN, USA

[*] Address all correspondence to Xianfan Xu E-mail: xxu@purdue.edu

The photoacoustic (PA) technique is one of many techniques for characterizing thermal conductivity of materials, including thermal interface conductance or resistance. Compared with other techniques, the PA method is relatively simple, yet is able to provide accurate thermal conductivity data over a wide range of materials and properties. In the last decade, the PA method has been developed and employed for measuring thermal properties of many materials. In this chapter, we will discuss the theory of the PA method for thermal conductivity/thermal interface resistance measurement. We will also describe experimental implementation of the PA method. Finally, we will discuss a recent application of using the PA method for characterizing thermal interface resistance of carbon nanotube–based thermal interface materials.

1. THEORY OF THE PHOTOACOUSTIC METHOD FOR THERMAL PROPERTY MEASUREMENTS

When a pulsed or periodically modulated light irradiates the surface of a solid, a number of thermomechanical phenomena can occur simultaneously. An acoustic wave can be generated in the gas adjacent to the material irradiated by the light due to the increase in pressure in the gas near the material's surface, which is termed the photoacoustic (PA) phenomenon. For thermal property measurement, this pressure wave is measured and related to the temperature of the gas and the solid near the gas-solid interface, as well as the thermal properties of the solid material(s). In addition, a thermomechanical/stress wave can be generated in the solid due to thermal expansion. The PA wave in the gas and the thermomechanical wave in the solid vary with the duration of the light pulse due to different thermal phenomena associated with different heating times. When the duration of the light pulse is nanosecond or longer, the PA wave in the gas is relatively strong due to the heat conduction from the solid, while the thermomechanical wave in the solid can be relatively weak due to the slow thermal expansion.

ISSN: 1049–0787; ISBN: 978–1–56700–222–6/13/$35.00 + $00.00

© 2013 by Begell House, Inc.

NOMENCLATURE

a	$1/\mu$ thermal diffusion coefficient	U, V	intermediate coefficient matrix
A	amplitude, intermediate coefficient	V	volume
B	function of variable physical properties, intermediate coefficient		
c	constant	**Greek Symbols**	
c_p	specific heat	α	thermal diffusivity
E, G	intermediate parameter	β	optical absorption coefficient
f	modulation frequency	θ	modified temperature
I	intensity of laser light	λ	wavelength of laser
j	$\sqrt{-1}$ imaginary unit	μ	$\sqrt{2\alpha/\omega}$ thermal diffusion length
k	thermal conductivity	σ	$(1 + j)a$, thermal penetration depth at a given frequency, standard deviation
l	depth of the cell	ϕ	phase shift
L	thickness of the cell	ω	modulated angular frequency
N	layer number		
p	pressure, property value	**Subscript**	
R	thermal contact resistance	i	layer i in the multilayer system
S	sensitivity		

The PA phenomenon has been studied for many decades, and has been used in nondestructive materials detection and thermophysical property measurements. A quantitative understanding of the PA effect was first given by Rosencwaig and Gersho, known as the RG model.[1] Since then, many extensions and applications of the RG model have been developed, basically into two directions. One was to further study the basic mechanism of the PA effect. By including mechanical vibration of the sample surface, McDonald and Wetsel presented a composite piston model, which was especially important for liquids due to its large thermal expansion.[2] The other attempt was to generalize Rosencwaig and Gersho's work to multilayer materials.[3–6] In a general case of a multilayer material, light can be absorbed by the layers beneath the surface, even by the backing material (the substrate). General mathematic models of the PA effect considering light absorption in a multilayer material and thermal contact resistances between layers were developed by Hu et al.[7] and Wang et al.[8] A more recent work by Hu et al. considered coupled thermal-mechanical phenomena;[9] however, the energy generated by mechanical work in a PA measurement is typically very small. The PA methods discussed below are based on Hu et al.[7] and Wang et al.[8]

1.1 Solution of the Heat Transfer Problem in the Photoacoustic Method

The temperature variation in the gas in a PA experiment is due to two effects: one is heat conduction through contact with the solid surface, the other is the mechanical work imposed on the gas medium due to vibration of the solid surface. For most solid materials

of interest, heat conduction from solid is dominant, and is considered in the following derivations.

Consider a multilayer material with a cross-sectional view as shown in Fig. 1. The light source is assumed to be a sinusoidally modulated monochromatic laser beam of wavelength λ, incident through nonabsorbing gas on the solid with a flux of $I = 1/2 \cdot I_0(1 + \cos\omega t)$, where ω is the modulation angular frequency of the incident light. The sample is composed of N layers with indices 1 through N. The indices of the substrate material and the gas are 0 and $N + 1$, which also take the subscripts b and g, respectively. Layer i has a thickness of $L_i = l_i - l_{i-1}$, thermal conductivity k_i, specific heat c_{p_i}, thermal diffusivity α_i, and optical absorption coefficient β_i, where i = 0, 1, ..., N + 1.

Other parameters used are the thermal diffusion length $\mu_i = \sqrt{2\alpha_i/\omega}$, the thermal diffusion coefficient $a_i = 1/\mu_i$, and the thermal contact resistance between layers i and $(i + 1)$, $R_{i,i+1}$. The thermal diffusion equation in layer i can then be expressed as

$$\frac{\partial^2\theta_i}{\partial x^2} = \frac{1}{\alpha_i}\frac{\partial\theta_i}{\partial t} - \frac{\beta_i I_0}{2k_i}\exp\left(\sum_{m=i+1}^{N} -\beta_m L_m\right)\cdot\exp[\beta_i(x - l_i)](1 + e^{j\omega t})$$
$$(l_{i-1} < x < l_i) \tag{1}$$

where $\theta_i = T_i - T_{\text{amb}}$ is the modified temperature in layer i, and T_{amb} is the ambient temperature. The solution θ_i of the above thermal diffusion equation set consists of three parts: the transient component $\theta_{i,t}$, which reflects the temperature variation at the early stage of laser heating, the final temperature elevation due to the laser heating, $\bar{\theta}_{i,s}$, and the steady transient component $\tilde{\theta}_{i,s}$, which varies with time periodically. Therefore,

$$\theta_i = \theta_{i,t} + \bar{\theta}_{i,s} + \tilde{\theta}_{i,s} \tag{2}$$

In a PA measurement, only the component periodically varying with time is measured, therefore, only $\tilde{\theta}_{i,s}$ needs to be evaluated. $\tilde{\theta}_{i,s}$ is resulted from the periodical source term (the last term on the right-hand side) in Eq. (1). With this source term, Eq. (1) has a particular solution in the form of $-E_i\exp[\beta_i(x - l_i)]\exp(j\omega t)$, with $E_i = G_i/(\beta_i^2 - \sigma_i^2)$,

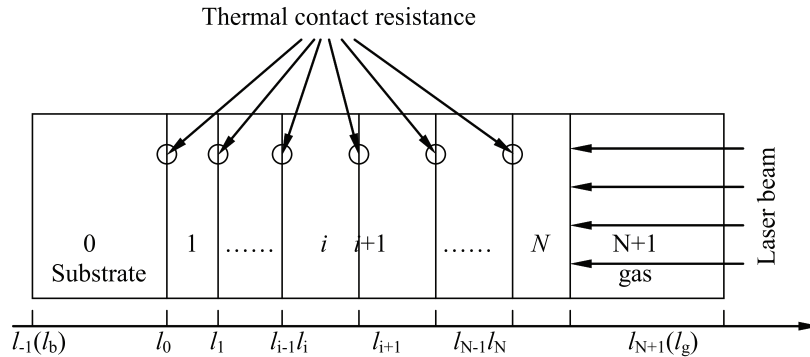

FIG. 1: Illustration of a multilayer sample irradiated by a laser beam.

$G_i = \beta_i I_0/(2k_i) \exp\left(-\sum_{m=i+1}^{N} \beta_m L_m\right)$ for $i < N, G_N = \beta_N I_0/(2k_N)$, and $G_{N+1} = 0$. σ_i is defined as $(1+j)a_i$ with $j = \sqrt{-1}$. The general solution of $\tilde{\theta}_{i,s}$ can be expressed in the form of

$$\tilde{\theta}_{i,s} = \left[A_i e^{\sigma_i(x-h_i)} + B_i e^{-\sigma_i(x-h_i)} - E_i e^{\beta_i(x-h_i)}\right] \cdot e^{j\omega t} \tag{3}$$

where h_i is calculated as $h_i = l_i$ for $i = 0, 1, ..., N$, and $h_{N+1} = 0$.

In most PA experiments, the gas and the substrate layer are thermally thick, meaning $|\sigma_0 L_0| \gg 1$ and $|\sigma_{N+1} L_{N+1}| \gg 1$, and the coefficients A_{N+1} and B_0 can be taken as zero.[8] The rest of the coefficients A_i and B_i are determined by applying the interfacial conditions at $x = l_i$,

$$k_i \frac{\partial \tilde{\theta}_{i,s}}{\partial x} - k_{i+1} \frac{\partial \tilde{\theta}_{i+1,s}}{\partial x} = 0 \tag{4}$$

$$k_i \frac{\partial \tilde{\theta}_{i,s}}{\partial x} + \frac{1}{R_{i,i+1}} (\tilde{\theta}_{i,s} - \tilde{\theta}_{i+1,s}) = 0 \tag{5}$$

Using a recurrence approach, the final expression of the temperature distribution $\tilde{\theta}_{i,s}$ in layer i is expressed as[8]

$$\begin{aligned} \tilde{\theta}_{i,s} = e^{j\omega t} \cdot \Bigg\{ & \left[\begin{array}{cc} e^{\sigma_i(x-h_i)} & e^{-\sigma_i(x-h_i)} \end{array}\right] \\ & \cdot \left(B_{N+1} \left(\prod_{m=i}^{N} U_m \right) \left[\begin{array}{c} 0 \\ 1 \end{array}\right] + \sum_{m=i}^{N} \left(\prod_{k=i}^{m-1} U_k \right) V_m \left[\begin{array}{c} E_m \\ E_{m+1} \end{array}\right] \right) - E_i e^{\beta_i(x-h_i)} \Bigg\} \end{aligned} \tag{6}$$

The expressions of the terms in Eq. (7) can be found in Ref. 8. In particular, the periodically varying temperature distribution in the gas is

$$\tilde{\theta}_{N+1,s} = B_{N+1} e^{-\sigma_{N+1} x} e^{j\omega t} \tag{7}$$

1.2 Temperature and Pressure/Acoustic Signal Relation in Photoacoustic Measurements

The pressure wave measured in the PA method is the pressure oscillation in the gas. The total differential pressure of the gas can be represented as

$$dp = \left(\frac{\partial p}{\partial T}\right)_V dT + \left(\frac{\partial p}{\partial V}\right)_T dV \tag{8}$$

With the ideal gas assumption,

$$\left(\frac{\partial p}{\partial T}\right)_V = \frac{p}{T}, \quad \left(\frac{\partial p}{\partial V}\right)_T = -\frac{p}{V} \tag{9}$$

The design of a PA cell requires $L_g < \Lambda_s/2$; thus, p is uniform in the gas cell. However, there is a temperature distribution in the gas. For this reason, Eq. (9) can be rearranged as

$$dp = \frac{p}{T}\langle dT\rangle - \frac{p}{V}dV \tag{10}$$

where $\langle dT\rangle$ is the volumetric average of temperature variation of the gas in the cell. Physically, dp produces the acoustic signal. $dT = \tilde{\theta}_{N+1,s} + \delta\tilde{\theta}_{N+1,s}$, $dV = -\Delta V_s$ with ΔV_s the volumetric thermal expansion of the solid surface, $p = p_{\text{amb}}$, $T = T_{\text{amb}}$, and $V = V_g$, the total volume of the gas cell. Therefore, Eq. (11) can be rewritten as

$$dp = \frac{p_{\text{amb}}}{T_{\text{amb}}}\left\langle\tilde{\theta}_{N+1,s}\right\rangle + \left[\frac{p_{\text{amb}}}{V_g}\Delta V_s + \frac{p_{\text{amb}}}{T_{\text{amb}}}\left\langle\delta\tilde{\theta}_{N+1,s}\right\rangle\right] \tag{11}$$

The first term on the right-hand side of Eq. (12) represents the thermal piston effect resulted from the thermal expansion of the gas heated by the solid, which only occurs in a narrow layer in the gas adjacent to the sample surface and pushes the rest of the gas just like a piston. The terms in the bracket can be interpreted as a result of the mechanical piston effect due to the thermal expansion of the sample. The pressure variation caused by the thermal piston, dp_t, is calculated by averaging the temperature change in the gas as

$$dp_t = \frac{p_{\text{amb}}}{T_{\text{amb}}}\left\langle\tilde{\theta}_{N+1,s}\right\rangle = \frac{p_{\text{amb}}}{T_{\text{amb}}L_g}\int_0^{L_g} B_{N+1}e^{-\sigma_{N+1}x}dx \cdot e^{j\omega t} \tag{12}$$

$$= \frac{p_{\text{amb}}B_{N+1}}{\sqrt{2}T_{\text{amb}}L_g a_g}e^{j[\omega t-(\pi/4)]} \tag{13}$$

The pressure variation caused by the mechanical piston, dp_m, is calculated as

$$dp_m = \frac{p_{\text{amb}}}{V_g}\Delta V_s + \frac{p_{\text{amb}}}{T_{\text{amb}}}\left\langle\delta\tilde{\theta}_{N+1,s}\right\rangle = \frac{p_{\text{amb}}}{L_g}\Delta x_s + \frac{p_{\text{amb}}}{T_{\text{amb}}}\left\langle\delta\tilde{\theta}_{N+1,s}\right\rangle \tag{14}$$

However, it can be estimated that $|dp_m/dp_t| > 1\%$.[8] Thus, the mechanical piston effect can be neglected, and the pressure variation in gas is only related to the thermal piston effect.

According to Eq. (13), the phase shift of the PA signal is $\text{Arg}(B_{N+1}) - \pi/4$, where Arg is the angle for the complex number B_{N+1}, and the amplitude can be calculated as $\left|p_{\text{amb}}B_{N+1}/\sqrt{2}T_{\text{amb}}L_g a_g\right|$. These two expressions are used in the derivation of the thermal properties from the measured phase and amplitude data.

2. IMPLEMENTATION OF THE PHOTOACOUSTIC METHOD FOR THERMAL PROPERTY MEASUREMENTS

2.1 Experimental Setup

A typical experimental setup of the PA method is shown in Fig. 2. A laser is used as the heating source, and its output is modulated by a lock-in amplifier. The output power of

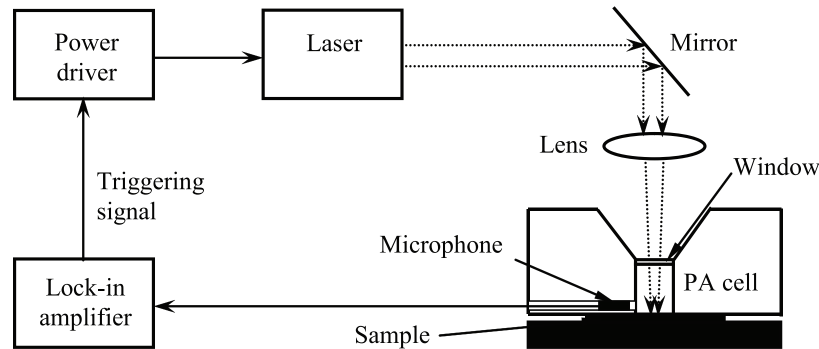

FIG. 2: Schematic of the PA experiment setup.

the diode laser is around a few hundred milliwatts at the modulation mode. After being reflected and focused, the laser beam is directed onto the sample mounted at the bottom of the PA cell. During the experiment, the maximum temperature rise at the sample surface is $<0.5°C$. A condenser microphone, which is built into the sidewall of the PA cell, senses the acoustic signal and transfers it to the lock-in amplifier, where the amplitude and phase of the acoustic signal are measured. A personal computer, which is connected to the GPIB interface of the lock-in amplifier, is used for data acquisition and control of the experiment.

The PA cell used in our work is a cylindrical, small volume, resonance-free cell made of highly polished acrylic glass and a sapphire window. Both acrylic glass and sapphire have low reflection and high transmission for the laser beam used, so most of the laser beam reflected from the sample surface transmits out of the cell. At a frequency of 20 kHz, the wavelength of the acoustic wave is $\sim$17.4 mm. In order to avoid resonance in the cell, the characteristic cell size has to be <8.7 mm. Therefore, the cell is designed to have an axial bore and height of a few millimeters in dimension. On the other hand, the smallest size of the cell is limited by the dimension of the microphone. The side of the bore facing the laser beam is sealed by a sapphire window, and the other side is sealed by the sample with an O-ring.

2.2 System Calibration

Due to the transfer function of the PA signal, which includes the time for the acoustic wave to reach the microphone and the delay of the electronic circuitry, the true PA signal is overlaid with additional signals. In order to remove these additional signals, reference samples of known thermal properties need to be used for calibration. These references can be polished graphite, single-crystal silicon wafer, and glass. A thin metal coating such as 70 nm–thick nickel is needed for all references and samples to absorb the laser energy. The reference samples are thick enough to be considered as bulk materials, and the phase shift is –90 deg. After the phase shift of the reference, ϕ'_{ref}, is obtained, the true phase shift of the sample, ϕ, is calculated as $\phi = \phi' - \phi'_{ref} - 90$, where ϕ' is the measured phase shift for the sample. The amplitude of the sample signal needs to be normalized with the

reference signal since its absolute value is difficult to obtain. The normalized amplitude of the sample, A, is calculated as $A = A'/A'_{\mathrm{ref}} \cdot A_{\mathrm{ref}}$, where A' is the measured amplitude, A'_{ref} is the measured amplitude for the reference e, and A_{ref} is the amplitude for the reference calculated using the theory in the previous section.

A common practice is to approximate the sample or the reference as thermally thick with a thickness t of 3σ, where σ is the thermal penetration depth at a given frequency. Silicon has a relatively high thermal diffusivity (8.9×10^{-5} m^2/s) such that the ability to use a silicon wafer as a reference will be dependent on its thickness and the modulation frequencies used. Figure 3 shows the measured phase shift of a 3 mm–thick quartz reference and a 380 μm–thick silicon reference over a frequency range of 200–3200 Hz. The 3σ thickness of silicon is plotted as well. Because the quartz reference is completely thermally thick at 3 mm, any other thermally thick reference sample should have the same measured phase shift as the quartz. As the modulation frequency increases, the penetration depth decreases and the silicon reference approaches thermal thickness. The thickness is equal to three times the penetration depth at a frequency of 1770 Hz. A silicon wafer would have to be 920 μm thick to fully satisfy the $t = 3\sigma$ criteria at a frequency of 300 Hz. Clearly, care must be taken when using a silicon reference, especially at lower frequencies.

The experimental setup is calibrated before any measurement. At each frequency, the signal needs to be allowed to stabilize first; then, data are taken. The phase shift and amplitude data are averaged. A computer code determines whether the variation of the average phase shift over a given time span is <0.2 deg, and the relative variation of the average amplitude is $<0.5\%$. Data are stored when the above criteria are reached. In order to determine the drift of the signals with time, the references are also measured after each sample measurement. A least-squares fitting procedure is used to determine the unknown properties such as thermal conductivity and thermal contact resistance.

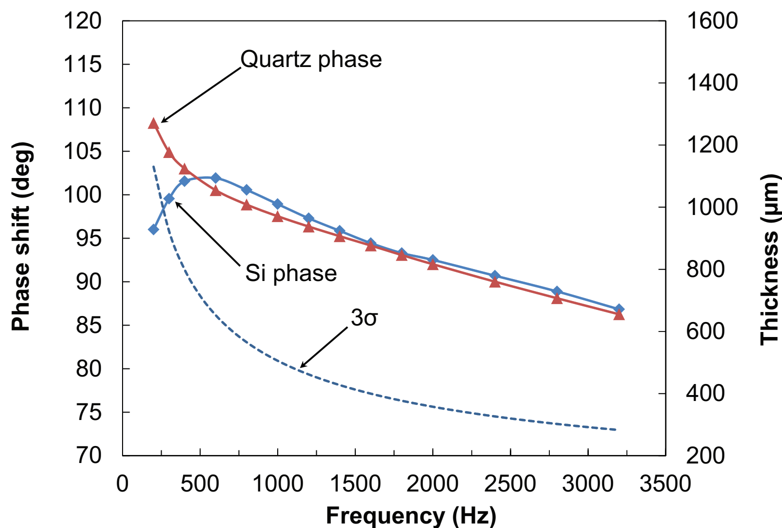

FIG. 3: Phase shift of a 3 mm–thick quartz reference compared to a 380 μm–thick silicon, and thickness of a thermally thick silicon wafer.

2.3 Other Considerations in PA Measurement

In system calibration, the phase shift is induced by the transfer function of the PA system, including the time delay of equipment (power supply of the diode laser, function generator, and microphone). Another very important factor that gives rise to the system time delay is the time taken for the acoustic wave to propagate to reach the microphone. This time delay is directly related to the relative position of the focused laser spot to the microphone. Therefore, in the experiment, the relative position of the laser spot to the microphone needs to be kept consistent. In the PA experiment, part of the PA wave will reach the microphone directly without reflection, and part of the PA wave will reach the inside wall of the PA cell, and experience multiple reflections before it reaches the microphone. Therefore, it is important that the inside wall of the PA cell has very little reflection or absorption of the PA wave.

3. PHOTOACOUSTIC MEASUREMENT OF CARBON NANOTUBE THERMAL INTERFACE MATERIALS

The PA method has been used for measuring thermal conductivity of thin films and bulk materials.[7,8,10] In recent years, an important application of the PA technique is for characterizing thermal interface materials (TIMs) with relatively low resistances, particularly carbon nanotube (CNT) array TIMs.[11−20] Compared to other techniques to measure thermal conductance across thin films and surface contacts, the PA technique is relatively simple, yet it provides high accuracy.[3,7,8,16,21−23] The measurement techniques that have been used in prior work to characterize CNT array interfaces have limitations that include one if not all of the following: the inability to measure resistances on the order of 1 mm^2 K/W or less precisely, the inability to individually resolve all the constitutive components of the total CNT interface resistance, and the inability to easily control the interface pressure and temperature during measurement. These limitations can be overcome using the PA technique and an appropriate sample configuration. In this section, we will discuss the steps required to implement the PA technique for measurement of CNT array thermal interfaces, and we will present several sets of data that demonstrate the capabilities of the PA technique as a useful TIM metrology.

3.1 Measurement Setup and Sample Configuration

The experimental setup for PA measurements is the same as shown in Fig. 2. Additional features of the setup for TIM measurement[14] are that the PA cell is pressurized by flowing compressed helium (He), thus providing a uniform average pressure on the sample surface. The PA cell pressure is adjusted using a flow controller and is measured by a gauge attached to the flow line. The relatively high thermal conductivity of He, compared to air, nitrogen, or argon, for example, produces a strong signal-to-noise ratio. A heater and thermocouple are embedded near the surface of the sample stage and are connected in a feedback system to control temperature. The embedded thermocouple is calibrated to the interface temperature by placing a second thermocouple in the interface of the sample and recording both thermocouple readings at each test temperature and pressure. The maximum test pressures

as well as the maximum and minimum test temperatures are limited by the tolerances of the microphone.

A schematic of an interface with a CNT array grown on one side (i.e., a one-sided CNT interface) is shown in Fig. 4 along with the labeling of layers used in the PA model discussed in Section 1.1. A schematic of the reference silicon is also shown in Fig. 4(b). The resistances of two-sided CNT interfaces[16,20] and CNT-coated foil interfaces[18,19] have also been measured with the PA technique; however, here, we focus on one-sided structures, which provide sufficient data to illustrate the merits and limitations of the technique.

We have found repeatedly that using the phase-shift data for CNT interfaces provides better fits to the PA model than using the amplitude data. The phase-shift signal is also more stable in the experimental setup described above, which reduces measurement uncertainty. Calibration is always performed at each test pressure and temperature to account for pressure-dependent and/or temperature-dependent phase lags due to the experimental setup, as discussed in Section 2.

A thin metal foil with high thermal conductivity is used to form the top of the interface sample [see Fig. 4(a)] to maximize the sensitivity of the PA technique to interface and CNT array resistances. The metal foil is typically silver (Ag) or copper (Cu), and is coated, along with the reference sample, with 80 nm of titanium (Ti) by electron beam deposition to ensure that the same amount of laser energy is absorbed in the surface layer of the sample and reference. The Ag foil [hard, Premion 99.998% (metals basis); Alfa Aesar, Inc.] is typically 25 μm thick, and the Cu foil [Puratronic 99.9999% (metals basis); Alfa Aesar, Inc.] is typically 50 μm thick to minimize the thermal resistance of the top interface substrate and allow the laser-generated heat to diffuse through the interface completely. The bottom substrate can be any thermally thick material. Thermally thick silicon and silicon carbide (SiC) wafers, quartz, and metal blocks have been used as bottom substrates to simulate material combinations used in common TIM applications.

Sensitivity calculations, performed by varying the magnitude of the total CNT interface resistance (i.e., the two contact resistances plus the array resistance) in the PA model at different heating frequencies, are plotted in Fig. 5 to illustrate the theoretical upper and lower bounds of interface resistance that can be measured with either Ag or Cu foil as the

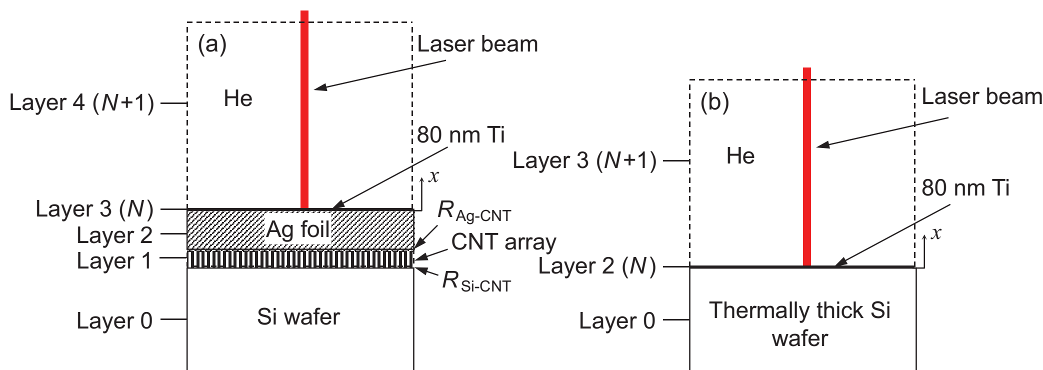

FIG. 4: Schematic of (a) one-sided CNT array interface test sample and (b) thermally thick reference sample configurations during PA measurement.[16]

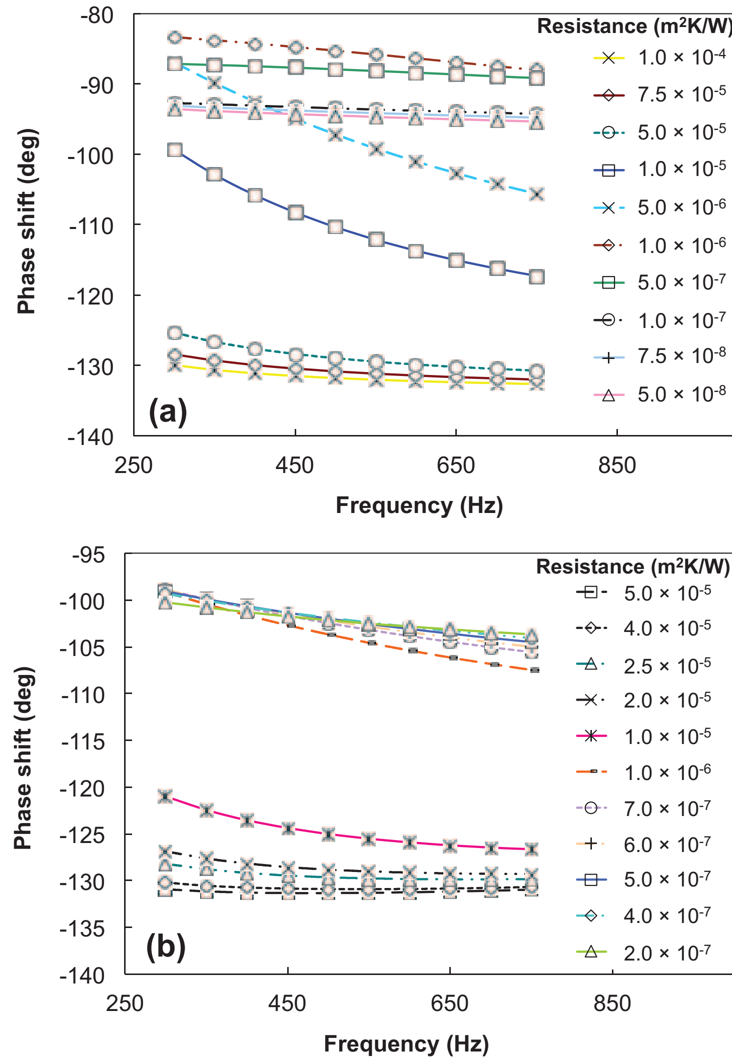

FIG. 5: Sensitivity calculations performed by varying the magnitude of the total CNT interface resistance in the PA model and calculating a theoretical phase shift at different heating frequencies. The limits are identified as the resistances at which additional changes in resistance alter the calculated phase shift little such that further changes fall within experimental uncertainty. (a) Sensitivity for Ag foil (25 μm thick) as the top substrate. (b) Sensitivity for Cu foil (50 μm thick) as the top substrate.[16]

top substrate material. The upper and lower PA contact resistance measurement limits are $\sim$100 mm^2 K/W and $\sim$0.1 mm^2 K/W, respectively, with Ag foil as the top substrate, and are $\sim$35 mm^2·K/W and $\sim$0.4 mm^2 K/W, respectively, with Cu foil as the top substrate. The use of the hard, 25 μm–thick Ag foil for measurements of interface materials instead of the 50 μm–thick Cu foil allows for greater measurement sensitivity. Cu foil of <50 μm

thick can improve measurement sensitivity as well; however, reduction in interface resistance resulting from the relatively soft foil conforming to the surface must be considered carefully in such a case. In general, the range of measurable resistances expands as the ratio of the thermal penetration depth to thickness increases for the top substrate. The upper measurement limit results when the effective thermal penetration depth of the sample is not sufficient to allow heat to pass through the interface and into the bottom substrate; the interface is thermally thick in this limit. The lower measurement limit results when the effective thermal penetration depth of the sample is much larger than the thermal thickness of the interface such that the interface is thermally thin. A 1D heat diffusion analysis is applicable for the sample configuration presented in Fig. 4(a) because at 300 Hz, the largest in-plane thermal diffusion lengths with Ag foil as the top substrate, 0.43 mm, and Cu foil as the top substrate, 0.35 mm, are much less than the laser beam size ($\sim$2 mm at its widest location).

3.2 Data Fitting

As discussed earlier in the chapter, the phase shift of the PA signal is $\text{Arg}(B_{N+1}) - \pi/4$, where B_{N+1} is a function of the densities, thermal conductivities, specific heats, thicknesses, optical absorption coefficients, and interface resistances in the multilayered sample. The known parameters in B_{N+1} are material properties that have been characterized by other measurement techniques, and/or are well documented in the literature. The unknown parameters in B_{N+1} are determined by fitting the PA model to the experimentally measured phase-shift data. It is possible to fit for a number of unknown material properties using PA measurements; however, the accuracy of the fit will improve as the number of unknowns is reduced. A typical practice is to fit for the thermal conductivity of a sample layer along with the two contact resistances between the sample layer and the adjacent layers. It is also possible to leave the density and/or specific heat of the sample layer as unknowns. This is typically done to improve the fitting and accuracy of the resistance values, rather than extract useful information about the density or specific heat of the sample.

When characterizing a multilayer sample with a number of unknown properties, there are a number of local minima to which a data-fitting algorithm will converge if the initial guess values are not close to the actual values. Fortunately, even a coarse data-fitting algorithm such as a sequential iterative minimization of the sum of the squares will accurately predict the bulk resistance of a sample (i.e., the sample resistance plus the two contact resistances). Significantly more care must be taken to resolve component resistances and thermal conductivities. We have found that the Levenberg-Marquardt (LM) nonlinear minimization algorithm provides good accuracy and efficiency for multiple parameter estimation using the model of Hu et al.[7] The LM method combines the steepest descent and inverse Hessian methods so that it may take large steps when far away from a minimum and smaller steps when approaching the minimum so as not to overshoot the final values.[24] Even when using this algorithm, accurate parameter estimation is strongly dependent on good initial guess values and reducing the number of unknowns. For an example of how the data fitting is influenced by unknowns, we consider a test

case of a one-sided CNT interface grown on silicon and in dry contact with Ag foil, as shown in Fig. 4(a). A theoretical phase-shift curve was calculated using assumed property values. This phase-shift curve is used as pseudo-experimental data that we attempt to fit using different guess values on a number of unknown parameters. The data fitting was performed using six, five, four, and three unknowns to examine how accurate the fitted parameters are compared to the actual input values. Table 1 lists the input values for each of the properties as well as the best-fit value for each of the four different fitting cases.

The accuracy of the estimated values is clearly much better for two or three unknowns compared to four, five, or six unknowns, and the exact values are predicted to within 1% only when two unknowns are used. It is interesting to note that even when the individual properties are not accurately predicted, the total resistance of the sample is estimated to an accuracy of 2%. This convergence occurs in spite of the fact that the initial guess is off by more than a factor of two. The bulk resistance is estimated more accurately than the layer properties because of the difference in sensitivity of the model to the various properties. The layer resistance of this hypothetical sample is 2 mm^2 K/W compared to contact resistances of 1 and 7 mm^2 K/W. Because the layer resistance is larger than contact resistance 2 (the contact between the CNTs and the silicon substrate), the parameter estimation works better for the layer thermal conductivity than the substrate contact resistance. For example, the error in prediction of R_{c2} for four and five unknowns is larger than the error in the thermal conductivity estimate. Six unknowns is a special case where two components of the layer resistance are allowed to vary (thermal conductivity and layer thickness). Treating both the thermal conductivity and thickness as unknowns is not recommended, and will often lead to largely erroneous estimations such as the extremely high thermal conductivity that was predicted for six unknowns. It should be mentioned that in practice, limits are set for each unknown parameter to keep estimated parameters within reasonable limits. For the purpose of this exercise, the limits were removed from the data fitting. It is important to note that even in the case of six unknowns, the theoretical curve matches the data extremely well with a very low residual. Figure 6 shows the data fit for the case of six unknowns.

TABLE 1: Accuracy of parameter estimation with different number of unknowns for a hypothetical one-sided CNT array interface (Si-CNT-Ag). The estimated parameters are in bold text

Data type	Thickness μm	Specific heat kJ/kg K	Density kg/m^3	Thermal conductivity W/m K	Contact resistance 1 mm^2 K/W	Contact resistance 2 mm^2 K/W	Total resistance mm^2 K/W
Initial guess	25.0	500	1500	10.0	12.00	3.00	17.50
Actual	40.0	750	1000	20.0	7.00	1.00	10.00
Six unknowns	**3.9**	**1559**	**4677**	**610,712.1**	**7.97**	**2.06**	10.03
Five unknowns	40.0	**692**	**2077**	**17.9**	**7.79**	**0.19**	10.21
Four unknowns	40.0	750	**1833**	**19.2**	**7.82**	**0.31**	10.21
Three unknowns	40.0	750	1000	**23.3**	**7.13**	**1.16**	10.01
Two unknowns	40.0	750	1000	**20.2**	**7.02**	1.00	10.00

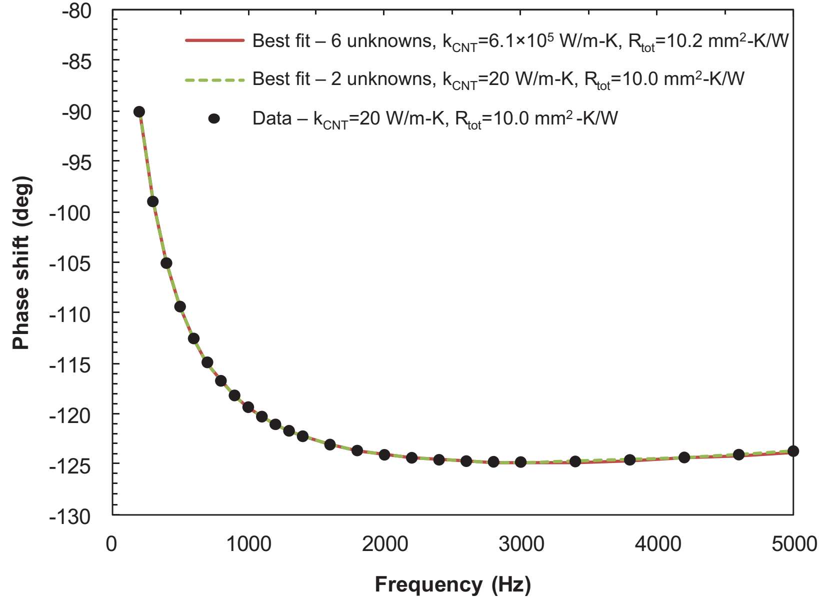

FIG. 6: Data fit for three- and six-unknown parameters.

3.3 Measurement Sensitivity, Uncertainty, Reproducibility, and Calibration

The ability of the PA method to estimate various parameters can be examined by looking at the sensitivity. We define the sensitivity as

$$S_p = \frac{\partial \phi}{\partial p} p \tag{15}$$

where we numerically calculate the partial derivative by perturbing the property value, p, by 1% to determine the change in phase, ϕ. The derivative is normalized by the property value, p, so that the sensitivity of properties that are orders of magnitude different can be directly compared. Given the manner in which the partial derivative is numerically calculated, it reduces to

$$S_p = 100 \cdot \partial \phi \tag{16}$$

which is similar to the sensitivity used by Hopkins et al.[25] for the transient thermoreflectance method. The difference is that Hopkins et al. normalized their sensitivity by dividing by the measured value. The measured phase-shift value is not relevant for normalizing in PA measurements. If it were desirable to normalize a phase shift, it would be more correct to normalize by 360 deg rather than the actual measured value to get a percentage. In any case, leaving the sensitivity in units of degrees has practical meaning for PA experiments, and because all measurements are between ± 180 deg, they are still directly comparable without normalizing.

One of the significant limitations in using the PA technique to resolve the thermal properties of a layer is that a high contact resistance in front of the layer will reduce the

sensitivity to the layer properties. To illustrate this point, we again consider the Si-CNT-Ag interface sample structure in Fig. 4(a). To determine the ability of PA to measure the thermal conductivity of the CNT layer, we can examine the sensitivity for different contact resistances between the CNT array and the silver foil (the height of the CNT array is fixed at 25 μm). Figure 7 shows the sensitivity of the phase to the thermal conductivity of the CNT array for contact resistances of 1, 2, 5, 10, and 20 mm^2 K/W at the CNT-Ag contact.

The sensitivity is plotted over a range of modulation frequencies from 100 Hz to 10 kHz, although a more typical range for PA measurements of TIMs might be 300 to 5 kHz. Figure 7 shows that the sensitivity to the layer thermal conductivity is strongly related to the contact resistance above the layer of interest. A 10-fold increase in the contact resistance from 2 to 20 mm^2 K/W results in a fivefold decrease in the sensitivity. It is also beneficial to use the sensitivity information to choose the proper frequency range to run an experiment. For a sample with an expected contact resistance of between 1 and 2 mm^2 K/W, spacing out data points from 300 Hz to 6 kHz would give a good sensitivity to the layer thermal conductivity, while it might make more sense to use more finely spaced frequencies between 200 Hz and 2 kHz for a sample with a contact resistance between 10 and 20 mm^2 K/W. To demonstrate the difference in sensitivity to the layer thermal conductivity, the phase shift of the CNT interface sample was plotted for resistances of 2 and 20 mm^2 K/W at the CNT-Ag contact. For both cases, the layer thermal conductivity was perturbed from its initial value of 25 W/m K by increasing and decreasing its value by a factor of two. The resulting phase shifts are displayed in Fig. 8. As expected from the sensitivity plot in Fig. 7, there is virtually no difference in phase shift when the front contact resistance is 20 mm^2 K/W, while there is an experimentally resolvable difference in the phase shift for different thermal conductivities when the front contact resistance is 2 mm^2 K/W.

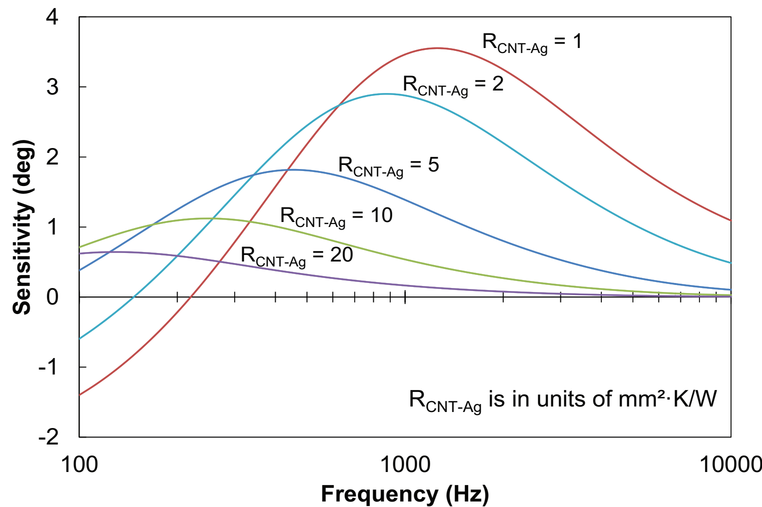

FIG. 7: Sensitivity of layer (i.e., the CNT array) thermal conductivity for different contact resistances above the layer (i.e., at the CNT-Ag contact). $R_{\mathrm{CNT-Ag}}$ has units of mm^2 K/W for each curve.

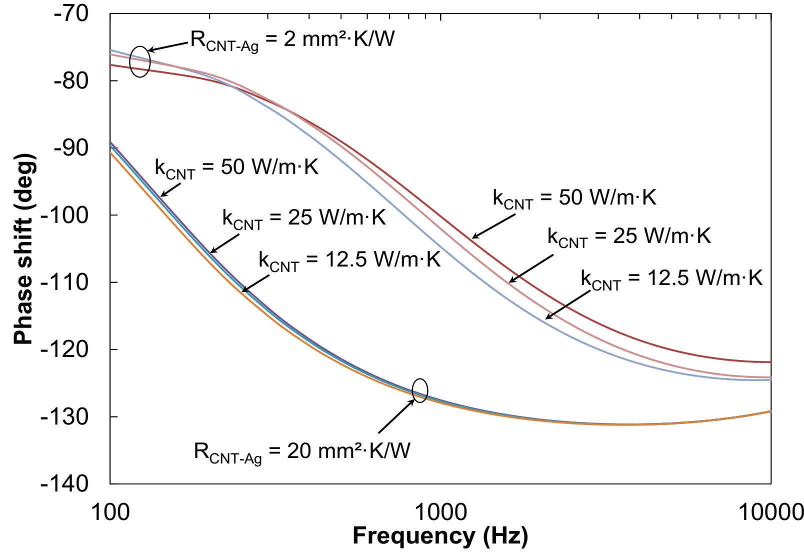

FIG. 8: Phase shift of CNT sample for various CNT-Ag contact resistances and CNT array thermal conductivities.

This is important to consider when reporting layer properties in a sample with high contact resistance.

Measurement uncertainty is determined primarily by the uncertainties associated with sensing the phase-shift signals. The highest uncertainties in measured phase shift for samples and references are usually of the order ±1.0 deg or less.[16] Uncertainty in the estimated thermal properties is determined by finding the range of property values that yield the phase-shift values within their experimental uncertainty range. Measurement uncertainties as low as 0.4 mm^2 K/W (or 10% of the measured value in this case) have been reported for PA measurement of CNT array interfaces.[16]

As with any measurement technique, periodic testing of a sample with known properties is critical to ensuring the accuracy and reproducibility of reported measurements. Silicon with a thermally grown oxide layer is one of the most commonly used calibration samples for the PA technique because it is easy to make, robust, and has well-documented thermal properties. Our standard sample is silicon (529 μm thick) with a layer of thermally grown silicon dioxide (SiO_2) that is 1 μm thick. 80 nm of Ti is deposited on top of the SiO_2 to absorb the laser energy. This sample is measured at regular intervals to ensure the proper operation of the PA measurements. This sample also provides a valuable indication of the measurement reproducibility of our PA cell. Table 2 contains a list of statistics from 25 measurements of thermal conductivity from the same SiO_2 sample over a three-month period, and Fig. 9(a) shows a histogram of the results. These measurements were performed at three different cell pressures (0, 69, and 138 kPa) with two different cell gases (air, He), which covers the typical operating range for our PA cell. The mean value of 1.46 W/m K is in good agreement with literature values for the thermal conductivity of thermally grown SiO_2 films[8,26] and bulk fused silica, 1.4 W/m K.[27] It is interesting to note that the

TABLE 2: Statistical summary of 25 measurements of the thermal conductivity of SiO_2 with the PA technique at regular intervals over a period of three months

Statistic	Value (W/m K)
Mean	1.459
Median	1.462
Standard deviation (σ)	0.075
2σ	0.150
50th–5th percentile	0.137
95th–50th percentile	0.126

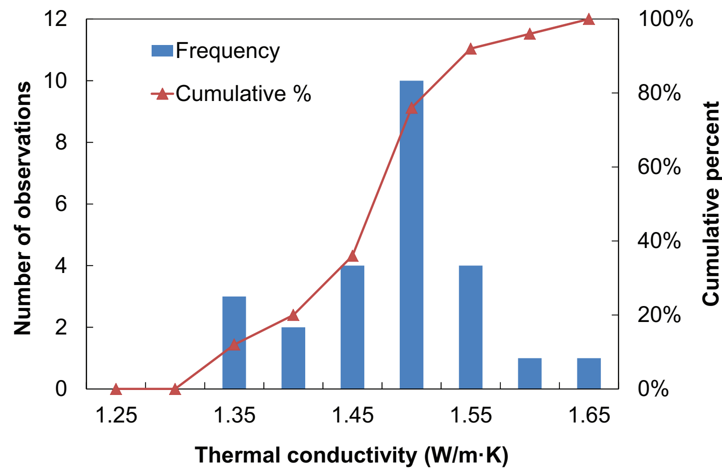

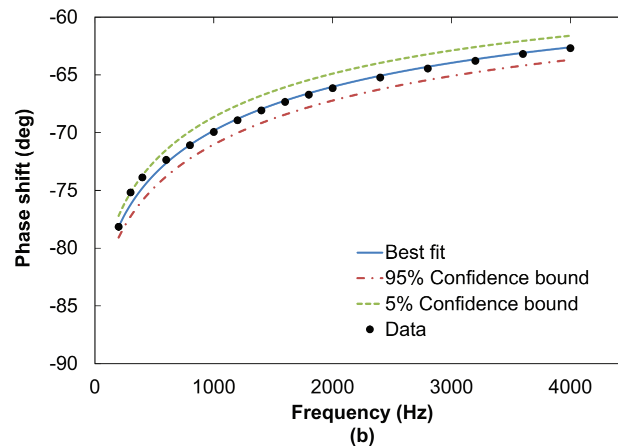

FIG. 9: (a) Histogram of SiO_2 thermal conductivity measurements. (b) Phase shift versus frequency for SiO_2, $k = 1.46 \pm 0.15$ W/m K.

50th–5th and 95th–50th percentiles are slightly smaller than two times the standard deviation. This indicates that the measurements are close to normally distributed, although the normal distribution slightly overestimates the variance in the data.

A 95% confidence interval of ±0.15 W/m K is excellent, considering the reported theoretical uncertainty for the measurement of an SiO_2 film on a comparable setup is ±0.08 W/m K (this value was determined by finding the range of property values that yield the measured phase-shift values within their experimental uncertainty range).[7] With the PA technique, it is likely that a significant degree of measurement variability results from the installation of the sample in the PA cell. The PA cell must be tightened down on the top of a sample for every measurement; this process could produce slightly different positions for the optical window depending on how well the cell is secured. The cell placement and tightening process also affects how well the cell is sealed to the sample, which can cause a noticeable difference in the measurement when the cell is pressurized. Figure 9(b) shows an example of the measured phase shift for a SiO_2 sample with the cell pressurized to 138 kPa with He. A well-characterized sample such as a thin film of SiO_2 is a very important quality check for any PA measurement.

The need to have all samples on a thermally thick backing is one of the drawbacks to the PA technique. This limitation can make measurements of calibration samples with thermal conductivities higher than SiO_2 challenging. In some cases, placing a sample in dry contact with a thermally thick backing that maintains a low contact resistance can circumvent the thermally thick requirement. Stainless steel foil (304) 50 μm thick was placed on a Parker Therm-A-Gap pad (Type G579) to demonstrate this approach. Figure 10 shows the experimental phase shift along with the best-fit theoretical curve. The unknown parameters were the thermal conductivity of the stainless steel and the contact resistances between the stainless steel and Ti transducer layer, and the contact resistance between the stainless steel and thermal pad. The fitted thermal conductivity was in excellent agreement with the published value and the contact resistances were within the expected range. An experimental uncertainty of ±1.1 deg in phase shift was used in determining the uncertainty in the fitted thermal properties. This uncertainty was derived from the SiO_2 data at a 95% confidence

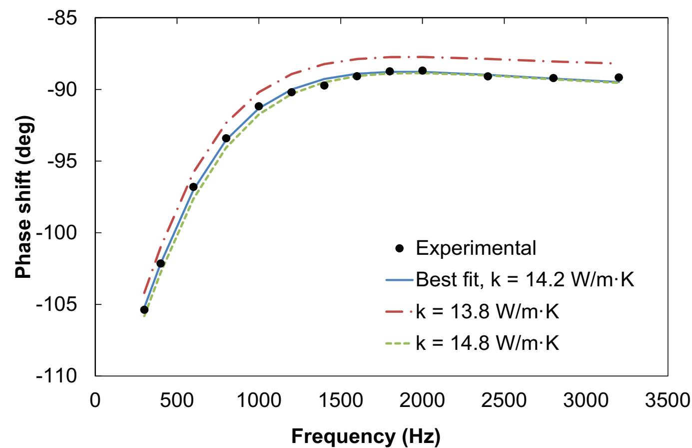

FIG. 10: Stainless steel foil in dry contact with a commercial thermal pad.

level. As illustrated in the plot, the lower bound on the data fit appears to be very similar to the best-fit line. This is an anomaly for this particular sample where both lower and higher thermal conductivities tend to have a larger phase shift than the value measured. The data fit for the minimum value is not as good as that for the best fit and maximum values, but was deemed acceptable as a confidence limit. Table 3 shows the parameter estimation based on the data in Fig. 10. It is interesting to note that because the higher contact resistance is behind the sample layer, the PA technique still has the capability to accurately resolve the thermal conductivity precisely.

3.4 Results of CNT TIM Contact Resistance Measurements

The PA technique is particularly attractive for its ability to identify bottlenecks to heat transport in CNT array interfaces. Figure 11 shows the intra-interface or component resistances of a one-sided Si-CNT-Ag interface with CNTs directly synthesized on silicon and in dry contact with Ag like the interface illustrated in Fig. 4. These resistances were measured with the PA technique at a contact pressure of 241 kPa.[16] The room temperature total thermal resistance of this interface was $\sim$16 mm^2 K/W. The resistance at the CNT-growth substrate interface ($R_{\mathrm{Si-CNT}}$) was $\sim$2 mm^2 K/W, and the resistance at the interface to the free CNT ends ($R_{\mathrm{CNT-Ag}}$) was approximately 14 mm^2 K/W. It is clear that the resistance between the free CNT ends and the Ag substrate dominated the overall thermal resistance, and that significant performance improvements can be achieved by reducing the resistance at this local interface.[16,17,28] Because of the high thermal conductivity and small thickness of the CNT array, its resistance could not be resolved using the PA technique in this experiment.[16]

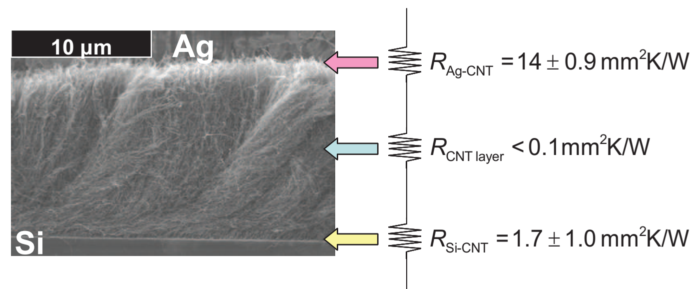

FIG. 11: Intra-interface resistances for a one-sided Si-CNT-Ag interface with CNTs directly synthesized on Si measured at room temperature and 241 kPa using the PA technique.[16]

TABLE 3: Fitted results from stainless steel foil in dry contact with a commercial thermal pad

Parameter	Fitted result	Uncertainty	Published value
k_{ss} (W/m K)	14.2	+0.6/–0.4	14.9
$R_{\mathrm{ss-ti}}$ (mm^2 K/W)	<0.1	±0.05	
$R_{\mathrm{pad-ss}}$ (mm^2 K/W)	8.0	+0.1/–0.2	

Figure 12 illustrates the ability of the PA technique to resolve small differences in thermal resistances for one-sided CNT interfaces (Si-CNT-Ag) at different test pressures.[13] The measured CNT arrays were grown at different temperatures, which produced different CNT array characteristics.[13] Both the average CNT diameters and the array heights decreased with decreased growth temperature. The increase in thermal resistance for shorter arrays with smaller CNT diameters was attributed to an increase in stiffness for such arrays. The resistance at the CNT-Ag contacts was found to be approximately equal to the total resistance of the interface for each tested array and at each test pressure. The ability to make PA measurements as a function of pressure as demonstrated in Fig. 12 was used recently in combination with a model for thermal transport in CNT array interfaces to reveal that the resistance of CNT array interfaces (R'') scales with pressure as $R'' \propto 1 + (c/P)$, where c is a constant based on CNT array properties and P is the applied contact pressure.[17] Therefore, the thermal resistance of CNT array interfaces becomes constant when $P \gg c$, which is consistent with the trends that can be observed in Fig. 12.

The PA technique has also been used to measure the thermal resistances of a CNT array interface grown on the C-terminated face of SiC in an elevated temperature range and at a contact pressure of 69 kPa.[14] The temperature-dependent thermal properties of all the layers in the sample and reference, and the gas in the PA cell (He), were required as inputs into the PA model. The resistances were measured at six different temperatures while heating the interface from room temperature to 250°C and while cooling the interface from 250°C to room temperature, as illustrated in Fig. 13(a). The SiC-CNT-Ag interface exhibited relatively little temperature dependence in the tested range. Illustrated in Fig. 13(b), other measurements in a similar elevated temperature range have been acquired for palladium (Pd) hexadecanethiolate bonded interface structures.[20] The bonded

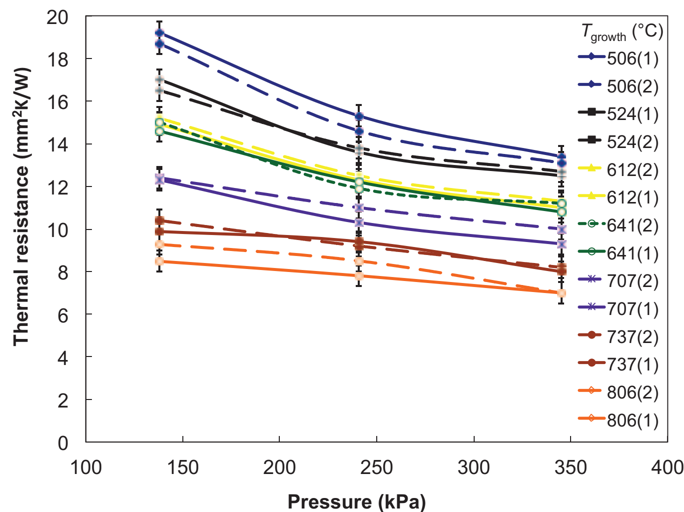

FIG. 12: Room temperature thermal resistances of Si-CNT-Ag interfaces as a function of pressure. CNT arrays were grown at different temperatures (two samples at each temperature), producing different array characteristics; the high precision of the PA technique enabled the effects of these differences on thermal resistance to be resolved.[13]

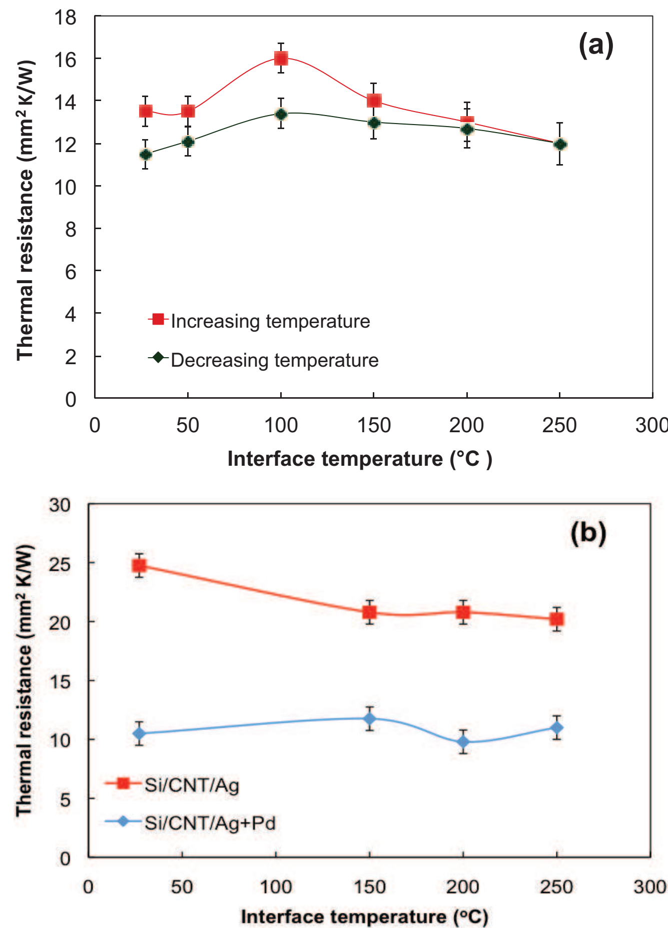

FIG. 13: PA measurements as a function temperature. (a) SiC-CNT-Ag interface at 69 kPa.[14] The CNTs were grown on the carbon-terminated face of SiC. The measurements were taken during heating and subsequent cooling of the interface. (b) Bulk thermal interface resistance as a function of interface temperature for a Si-CNT-Ag structure with and without Pd bonding.[20]

structure was Si-CNT-Ag, in which CNTs grown on silicon were bonded to Ag. At a contact pressure of 34 kPa, the resistances across the temperature range are relatively stable, indicating that the bonded interface structures are suitable for high-temperature applications.

In a study to elucidate the roles that CNT volume fraction and height have on thermal performance, PA measurements were taken on a series of Si-CNT-Ag structures that varied in average array height. The measurements were taken at contact pressures of 34 and 138 kPa at room temperature. Figures 14(a) and 14(b) compare thermal resistance to CNT volume fraction and height, respectively. The thermal resistance values are representative of the resistances at the free-tip CNT-Ag foil interface as locally resolved component

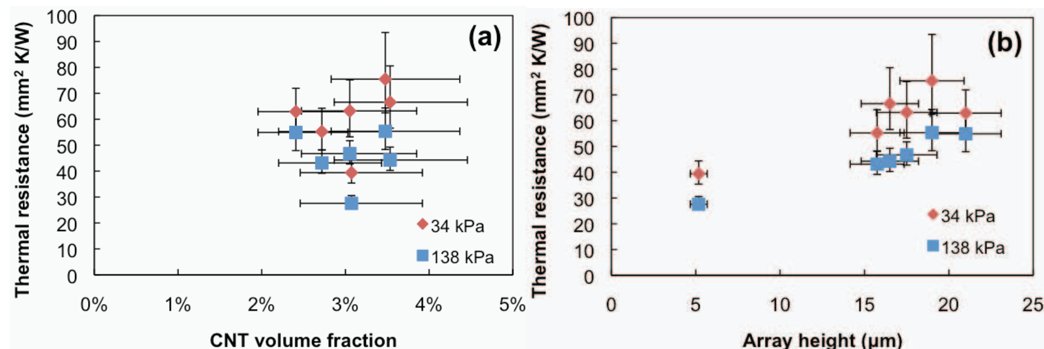

FIG. 14: Effects of CNT array characteristics on thermal resistance measured with PA for Si-CNT-Ag structure: (a) CNT volume fraction; (b) CNT array height.

resistances, and thermal diffusivities were fitted based on the volume fraction estimates for the array thermal conductivity, heat capacity, and density. Thermal resistances at the Si-CNT interface for all samples were <1 mm^2 K/W while thermal diffusivities of the CNT arrays ranged from 2.0 to 3.5×10^{-4} m^2/s. The thermal resistances show no correlation to CNT volume fraction, but do exhibit moderate correlations to array height, particularly at a higher contact pressure, with shorter arrays performing best. The absence of a correlation of thermal resistance to volume fraction is due to the narrow range of volume fractions and relatively large uncertainties associated with estimating the volume fraction, while the moderate dependence on array height corroborates the ability of the PA technique to reveal compressibility and roughness effects of the CNT array.

4. CONCLUSION

The photoacoustic method is shown to be a highly effective and precise technique for characterizing thermal conductivity and thermal interface resistances at mesoscopic length scales. As such, it is particularly well suited for a wide range of materials including thermal interface materials, which typically contain within them various hetero-interfaces as well as a solid or solidlike layer with finite but small thickness. The instrumentation does require a carefully constructed test cell with sensitive and precisely fabricated components, but the benefit is the resulting high precision and versatility for a class of thermal materials of increasing technological importance.

ACKNOWLEDGMENTS

B.A.C., S.L.H., T.S.F., and X.X.U. gratefully acknowledge partial support of this work from Raytheon as part of the DARPA Nano Thermal Interfaces Program. T.L.B. gratefully acknowledges fellowship support from the NSF IGERT: Nanomaterials for Energy Storage and Conversion program at Georgia Tech.

REFERENCES

1. A. Rosencwaig and A. Gersho, Theory of the photoacoustic effect with solids, *J. Appl. Phys.*, **47**:64–69, 1976.
2. F. A. Mcdonald and J. G. C. Wetsel, Generalized theory of the photoacoustic effect, *J. Appl. Phys.*, **49**:2313–2322, 1978.
3. N. C. Fernelius, Extension of the Rosencwaig-Gersho photoacoustic spectroscopy theory to include effects of a sample coating, *J. Appl. Phys.*, **51**:650–654, 1980.
4. Y. Fujii, A. Moritani, and J. Nakai, Photoacoustic spectroscopy theory for multi-layered samples and interference effect, *Jpn. J. Appl. Phys.*, **20**:361–367, 1981.
5. J. Baumann and R. Tilgner, Determining photothermally the thickness of a buried layer, *J. Appl. Phys.*, **58**:1982–1985, 1985.
6. S. D. Campbell, S. S. Yee, and M. A. Afromowitz, Applications of photoacoustic spectroscopy to problems in dermatology research, *IEEE Trans. Biomed. Eng.*, **BME-26**:220–227, 1979.
7. H. Hu, X. Wang, and X. Xu, Generalized theory of the photoacoustic effect in a multilayer material, *J. Appl. Phys.*, **86**:3953–3958, 1999.
8. X. Wang, H. Hu, and X. Xu, Photo-acoustic measurement of thermal conductivity of thin films and bulk materials, *J. Heat Transf.*, **123**:138–144, 2001.
9. H. Hu, W. Zhang, J. Xu, and Y. Dong, General analytical solution for photoacoustic effect with multilayers, *Appl. Phys. Lett.*, **92**:014103, 2008.
10. R. E. Taylor, X. Wang, and X. Xu, Thermophysical properties of thermal barrier coatings, *Surf. Coat. Tech.*, **120–121**:89–95, 1999.
11. P. B. Amama, B. A. Cola, T. D. Sands, X. Xu, and T. S. Fisher, Dendrimer-assisted controlled growth of carbon nanotubes for enhanced thermal interface conductance, *Nanotechnology*, **18**:385303, 2007.
12. P. B. Amama, C. Lan, B. A. Cola, X. Xu, R. G. Reifenberger, and T. S. Fisher, Electrical and thermal interface conductance of carbon nanotubes grown under direct current bias voltage, *J. Phys. Chem. C*, **112**:19727–19733, 2008.
13. B. A. Cola, P. B. Amama, X. Xu, and T. S. Fisher, Effects of growth temperature on carbon nanotube array thermal interfaces, *J. Heat Transf.*, **130**:114503, 2008.
14. B. A. Cola, S. L. Hodson, X. Xu, and T. S. Fisher, Carbon nanotube array thermal interfaces enhanced with paraffin wax, *ASME Conf. Proc*., ASME, New York, pp. 765–770, 2008.
15. B. A. Cola, R. Karru, C. Changrui, X. Xianfan, and T. S. Fisher, Influence of bias-enhanced nucleation on thermal conductance through chemical vapor deposited diamond films, *IEEE Trans. Compon. Packag. Technol.*, **31**:46–53, 2008.
16. B. A. Cola, J. Xu, C. Cheng, X. Xu, T. S. Fisher, and H. Hu, Photoacoustic characterization of carbon nanotube array thermal interfaces, *J. Appl. Phys.*, **101**:054313, 2007.
17. B. A. Cola, J. Xu, and T. S. Fisher, Contact mechanics and thermal conductance of carbon nanotube array interfaces, *Int. J. Heat Mass Transfer*, **52**:3490–3503, 2009.
18. B. A. Cola, X. Xu, and T. S. Fisher, Increased real contact in thermal interfaces: A carbon nanotube/foil material, *Appl. Phys. Lett.*, **90**:093513, 2007.
19. B. A. Cola, X. Xu, T. S. Fisher, M. A. Capano, and P. B. Amama, Carbon nanotube array thermal interfaces for high-temperature silicon carbide devices, *Nanoscale Microscale Thermophys.*, **12**:228–237, 2008.

20. S. L. Hodson, T. Bhuvana, B. A. Cola, X. Xu, G. U. Kulkarni, and T. S. Fisher, Palladium thiolate bonding of carbon nanotube thermal interfaces, *J. Electron. Pack.*, **133**:020907, 2011.
21. A. Lachaine and P. Poulet, Photoacoustic measurement of thermal properties of a thin polyester film, *Appl. Phys. Lett.*, **45**:953–954, 1984.
22. S. S. Raman, V. P. N. Nampoori, C. P. G. Vallabhan, G. Ambadas, and S. Sugunan, Photoacoustic study of the effect of degassing temperature on thermal diffusivity of hydroxyl loaded alumina, *Appl. Phys. Lett.*, **67**:2939–2941, 1995.
23. M. Rohde, Photoacoustic characterization of thermal transport properties in thin films and microstructures, *Thin Solid Films*, **238**:199–206, 1994.
24. W. H. Press, S. A. Teukolsky, W. T. Vetterling, and B. P. Flannery, *Numerical Recipes: The Art of Scientific Computing*, Cambridge University Press, Hong Kong, 2007.
25. P. E. Hopkins, J. R. Serrano, L. M. Phinney, S. P. Kearney, T. W. Grasser, and C. T. Harris, Criteria for cross-plane dominated thermal transport in multilayer thin film systems during modulated laser heating, *J. Heat Transfer*, **132**:081302, 2010.
26. M. Okuda and S. Ohkubo, A novel method for measuring the thermal conductivity of submicrometre thick dielectric films, *Thin Solid Films*, **213**:176–181, 1992.
27. A. F. Mills, *Basic Heat and Mass Transfer*, Irwin, Chicago, 1995.
28. T. Tong, Y. Zhao, L. Delzeit, A. Kashani, M. Meyyappan, and A. Majumdar, Dense vertically aligned multiwalled carbon nanotube arrays as thermal interface materials, *IEEE Trans. Compon. Packag. Technol.*, **30**:92–100, 2007.